



Article

Distribution and Characteristics of Damming Landslides Triggered by 1920 $M\sim 8$ Haiyuan Earthquake, NW China

Weiheng Zhang ^{1,2}, Yueren Xu ^{2,*} , Xinyi Guo ³, Wenqiao Li ², Peng Du ⁴ and Qinjian Tian ²

¹ State Key Laboratory of Earthquake Dynamics, Institute of Geology, China Earthquake Administration, Beijing 100029, China; zwh@ies.ac.cn

² Key Laboratory of Earthquake Prediction, Institute of Earthquake Forecasting, China Earthquake Administration, Beijing 100036, China; liwenqiao@ief.ac.cn (W.L.); tianqj@263.net (Q.T.)

³ Aerospace Information Research Institute, Chinese Academy of Sciences, Beijing 100094, China; guoxy@aircas.ac.cn

⁴ Guangdong Provincial Key Laboratory of Geodynamics and Geohazards, School of Earth Sciences and Engineering, Sun Yat-sen University, Zhuhai 519080, China; dupeng7@mail2.sysu.edu

* Correspondence: xuyr@ief.ac.cn

Abstract: Earthquake-triggered damming landslides threaten downstream residents and affect the regional landscape by disrupting water and sediment fluxes. Therefore, it is essential to study the distribution characteristics and distinctive controlling factors of earthquake-triggered damming landslides to provide a reference for treating landslide dams caused by damming landslides. This study uses the 1920 $M\sim 8$ Haiyuan earthquake-triggered landslides as an example to study the characteristics and topographic effects of damming landslides in the Loess Plateau in Northwestern China. A detailed Haiyuan-earthquake-triggered damming landslide inventory was established. The statistics of terrain, geology, seismic factors, and information gain rankings were used to quantify the significance of the controlling factors. The aspect ratio, equivalent coefficient of friction, area, and slope position was calculated. Damming landslides' distinctive geomorphic and morphological characteristics were summarized through comparisons with non-damming landslides. The results showed that damming landslides were concentrated in areas with thick loess sediment, low relief, and close proximity to a river. Loess thickness was the most critical control factor among them. Damming landslides have the geomorphological characteristics of a large ratio of length to width (L/W), a low ratio of height to length (H/L), large scales, and entire-slope failure. Moreover, damming landslides can transform the topography of the Loess Plateau through their long-term effects. These findings highlight the characteristics of damming landslides in the Loess Plateau and supplement the global landslide dam inventory. They provide a reference for assisting in earthquake-triggered damming landslides treatments in the Loess Plateau.

Keywords: 1920 Haiyuan $M\sim 8$ earthquake; earthquake-triggered landslides; damming landslides; Loess Plateau; geomorphological characteristics; landscape evolution



Citation: Zhang, W.; Xu, Y.; Guo, X.; Li, W.; Du, P.; Tian, Q. Distribution and Characteristics of Damming Landslides Triggered by 1920 $M\sim 8$ Haiyuan Earthquake, NW China. *Remote Sens.* **2022**, *14*, 2427. <https://doi.org/10.3390/rs14102427>

Academic Editors: Issaak Parcharidis, Fulong Chen and Olga Markogiannaki

Received: 11 April 2022

Accepted: 16 May 2022

Published: 18 May 2022

Publisher's Note: MDPI stays neutral with regard to jurisdictional claims in published maps and institutional affiliations.



Copyright: © 2022 by the authors. Licensee MDPI, Basel, Switzerland. This article is an open access article distributed under the terms and conditions of the Creative Commons Attribution (CC BY) license (<https://creativecommons.org/licenses/by/4.0/>).

1. Introduction

Landslides, as one of the most destructive geohazards, pose a severe threat to residents and property by destroying buildings, blocking roads and rivers, and causing other modes of damage. Some landslides block rivers and form landslide-dammed lakes (LDLs), and these are known as damming landslides. The accumulation of materials from damming landslides which block rivers are called landslide dams, which are generally loose and unstable. The potential flood hazard caused by a sudden break may bring catastrophic damage to a downstream area [1].

In April 2000, the Yigong landslide, located in SW China, blocked the Jinsha River and formed a LDL. In June of the same year, the landslide dam was broken, generating a substantial flood outburst downstream [2]. In 2018, the Baige landslide occurred along the

Jinsha River and blocked it. Although there was a rapid response to this slope failure, it still caused substantial economic losses, and more than 20,000 people in the downstream area were forced to migrate [3–5]. Similar events of landslide dam breaks are common in mountainous regions worldwide, including the Alps, Himalayas, the margin of the Tibetan Plateau, the Andes, and some mountainous countries, such as Italy, Japan, and New Zealand [6–10].

Earthquakes are one of several causes that trigger damming landslides. The rapid treatment of large landslide dams caused by damming landslides is the most challenging task in the post-earthquake rescue process, such as in the case of the Tangjiashan earthquake-triggered landslide dam after the 2008 M_w 7.9 Wenchuan earthquake [11] and the Hongshiyuan landslide dam after the 2015 M_s 6.5 Ludian earthquake [12]. This treatment process has aroused widespread social concern.

It is necessary to identify damming landslides and study the relationship between the distribution and controlling factors of damming landslides for predicting and preventing the occurrence of future dams triggered by earthquake-triggered damming landslides [13,14]. Common disaster identification methods based on remote sensing include [15–19]: (1) visual interpretation, (2) automated classification, and (3) field investigation. Although visual interpretation and field investigation can consume a lot of time, they are still the most effective and reliable methods to obtain objective data. Previous studies have also proven the feasibility of visual interpretation using recent remote sensing images to interpret historical earthquake-triggered landslides in the Loess Plateau (LP) [20–26].

The 1920 Haiyuan M ~8 earthquake (HYEQ) was one of the most destructive earthquakes in LP, NW China, and it triggered many landslides, including damming landslides [21,27–31]. These damming landslides caused enormous destruction during the earthquake [27,28]. They also changed the landscape during and after the earthquake. Because of the apparent trailing edge of landslides and well-reserved LDLKs, damming landslides triggered by the HYEQ can still be identified [21]. This provides a natural case for studying the distribution and characteristics of earthquake-triggered damming landslides in LP, NW China.

The statistical method is effective in studying landslide distribution characteristics [13,21,22,30–32]. Previous studies have analyzed the relationship between the overall distribution of HYEQ-triggered landslides and the controlling factors based on a statistical analysis of a detailed landslide inventory [21,30]. Other studies have investigated the failure mechanisms of some HYEQ-triggered landslides based on soil mechanical tests [33–35]. However, although previous studies have briefly introduced damming landslides and LDLKs [21,30], few have analyzed the distribution and characteristics of the study area's damming landslides in detail. There is also a lack of statistics on the detailed damming landslide geomorphic variables that are important in analyzing the stability and geomorphic evolution of damming landslides [10].

In this study, we identified damming landslides by visually interpreting Google Earth images from the HYEQ-triggered coseismic landslide inventory and verified the identification results through field investigation. The characteristics of the distribution and geometry of the HYEQ's damming landslides are summarized here by analyzing the factors controlling damming and non-damming landslides. Then, the main factors controlling damming landslides and the role of loess landslide dams in landscape evolution are discussed. Moreover, in this study we discuss the characteristics of landslide dams caused by damming landslides in the LP with those from the global database.

2. Study Area

The study area is located in the LP of Northwestern China in the transformation zone between the Tibetan Plateau and the Ordos Block, the deformation frontier in the accommodation of Indo-Asian convergence (Figure 1a). The region hosts many active faults, consisting mainly of a series of ~EW-trending left-lateral strike-slip faults, including

the Haiyuan fault, Altyn Tagh fault, Kunlun fault, and other conjugate right-lateral faults, with considerable off-fault deformation [36] (Figure 1b).

A 240 km-long surface rupture zone accompanied the 1920 $M\sim 8$ HYEQ along the Haiyuan Fault (HYF) with an approximately 5 m coseismic horizontal offset. The HYF is an approximately 1000 km long active, left-lateral structure in the northeastern Tibetan Plateau [37]. It is eastward of the Altyn Tagh fault in the Qilianshan Mountain range, with a strike of approximately 110° , with a further eastward turn to a 155° strike connected with the Liupanshan fault (LPSF) [38] (Figure 1c).

The HYEQ affected an area of more than $67,500\text{ km}^2$, killed more than 234,000 people, and caused widespread social disasters [21,27,39,40]. The damage caused by the earthquake has been effectively counted and reported in time. The post-earthquake investigation reports of various organizations specifically mentioned that a large number of loess landslides were triggered by this earthquake [21,27,28]. More than 7000 landslides can still be distinguished in the intersection area of the LPSF and HYF [21,22] (Figure 1c). The terrain in the study area gradually rises from west to east and from south to north [41]. The main landforms are loess hills. The Lanni River and Hulu River are the main rivers in the study area. The Lanni River is a tributary of the Hulu River, which is a secondary tributary of the Yellow River. Many damming landslides triggered by the HYEQ have subsequently existed for more than 100 years, which have substantially modified the landscapes in this region [21,30] (Figure 1d).

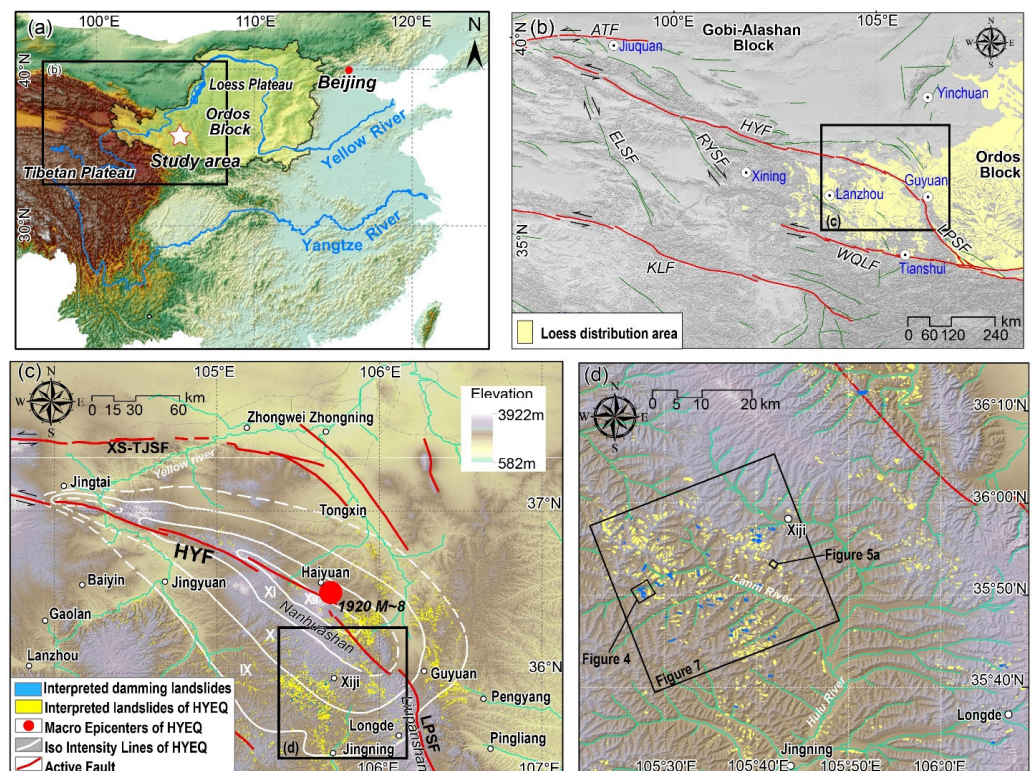


Figure 1. Distribution of interpreted landslides in the HYEQ influence area and the concentration areas of landslide dams (landslide data from Xu et al., 2021) [20,21]. (a) Location of the study area in China. (b) Loess and active faults in northeastern Tibetan Plateau. HYF: Haiyuan fault; ATF: Altyn Tagh fault; LPSF: Liupanshan fault; WQLF: West Qinling fault; KLF: Kunlun fault; ELSF: Elashan fault; RYSF: Riyueshan fault; (c) Distribution of interpreted landslide in the HYEQ-influenced area. HYF: Haiyuan fault; LPSF: Liupanshan fault; XS-TJSF: Xiangshan-Tianjingshan fault. (d) Concentration areas of damming landslides. Iso intensity lines based on the Lanzhou Institute of Seismology, SSB et al., 1980 [27]. Active faults based on 1:4,000,000 scale of the active faults in China [42].

3. Materials and Methods

In this study we explored the characteristics and implications of damming landslides triggered by the HYEQ in the LP. In order to achieve this goal, the following preparations were made: (1) constructing a damming landslide inventory and preparing to assess the controlling factors of HYEQ-triggered landslides; (2) analyzing the morphometry, spatial distribution, and information gain to summarize the morphometry features, abnormal distribution characteristics, and the important controlling factors; (3) summarizing and discussing the characteristics and landscape implications of damming landslides in LP. Figure 2 shows a flow chart of these efforts.

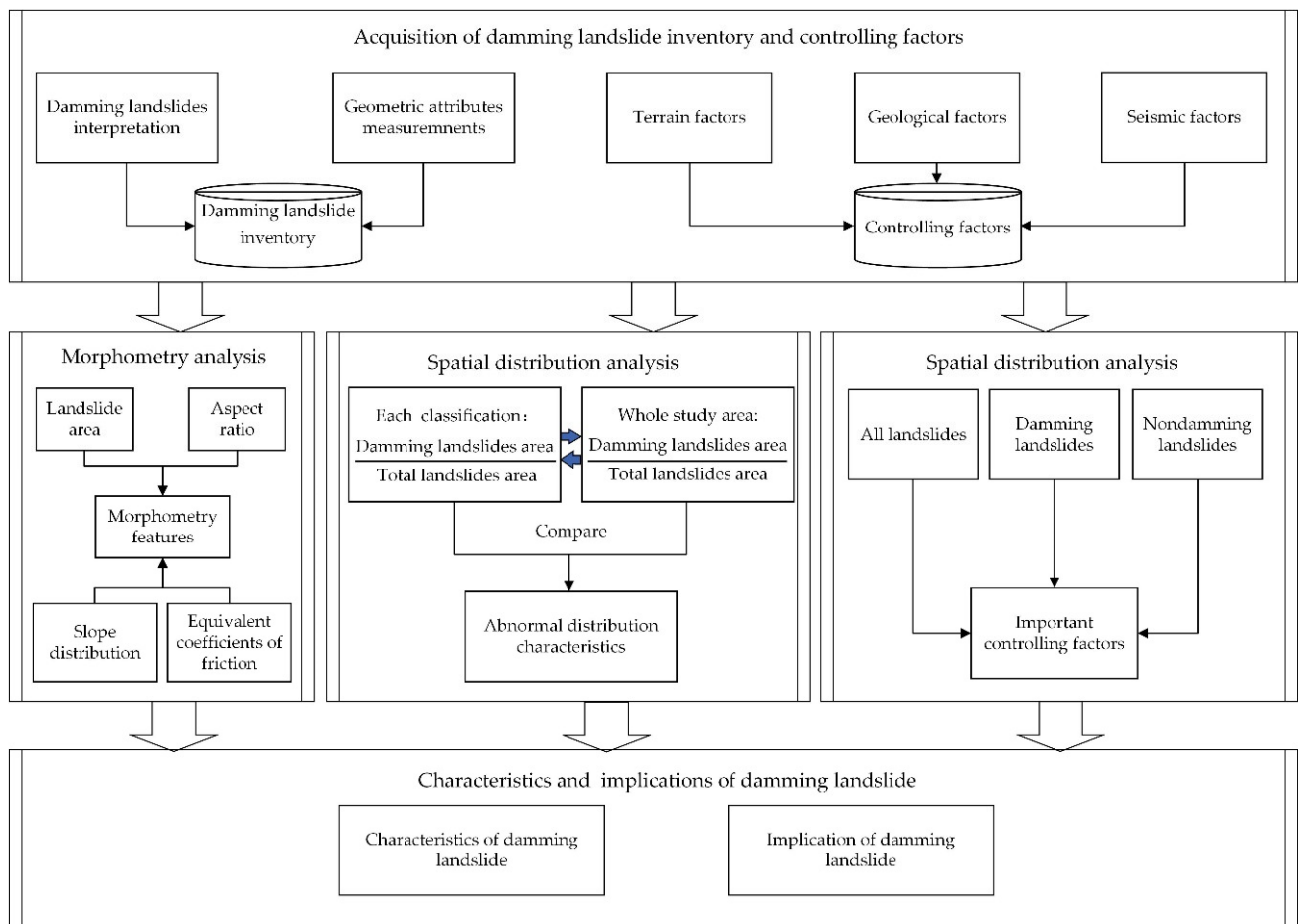


Figure 2. Procedural flow chart of this study.

3.1. Damming Landslide Inventory and Controlling Factor Preparation

The coseismic landslide inventory of the HYEQ, which spans a study area of 67,500 km², was extracted by interpreting multi-temporal high-resolution Google Earth images and verified by field investigations (Figure 1) [20,21]. The 1920 HYEQ-triggered landslides can be easily identified according to the material loss in the landslide area and the steep trailing scarp (Figure 3). Multi-temporal Google Earth images and UAV images show that the landslide morphometry was stable in the recent ~30 years. The landslide trailing scarp can be accurately identified on the Google Earth images (Figure 4). Previous works have proven the rationality and reliability of using recent Google Earth images to build the historical strong earthquake-triggered landslide inventory in the LP [20,21]. The HYEQ-triggered landslide inventory includes almost all large-scale (>10⁴ m²) and the majority of medium-small scale (10⁴ m²–10⁴ m²) HYEQ-triggered coseismic landslides [20,21]. It excludes the influence of landslides triggered by medium earthquakes, rainfall, human activities, and other factors in the study area [20–26]. Damming landslides were further

identified from the inventory [21] based on the following characteristics: (1) landslides, the well-reserved accumulation of which blocked the river and contained a lake within the upstream valley; (2) landslides, the accumulation of which was broken, reserving a flat and widened valley upstream of the abandoned landslide dam, and a deep valley downstream of the dam; and (3) landslides, the accumulation of which was modified to a reservoir dam. For each damming landslide, we calculated the length (L_L), width (W_L), area, and elevation of the landslide's top and toe, the elevation of the ridge above landslide (H_{ridge}), and the valley bottom below landslide (H_{stream}). For the catchment areas blocked by damming landslides, we counted the catchment area (A_C) and the maximum inundation range of the landslide-dammed lake (A_{dl}). For the dams caused by damming landslides, we counted dam height (H_D), length (L_D), width (W_D), and volume (V_D) (Figure 5). The complete statistical data are provided in the Supplementary Materials.

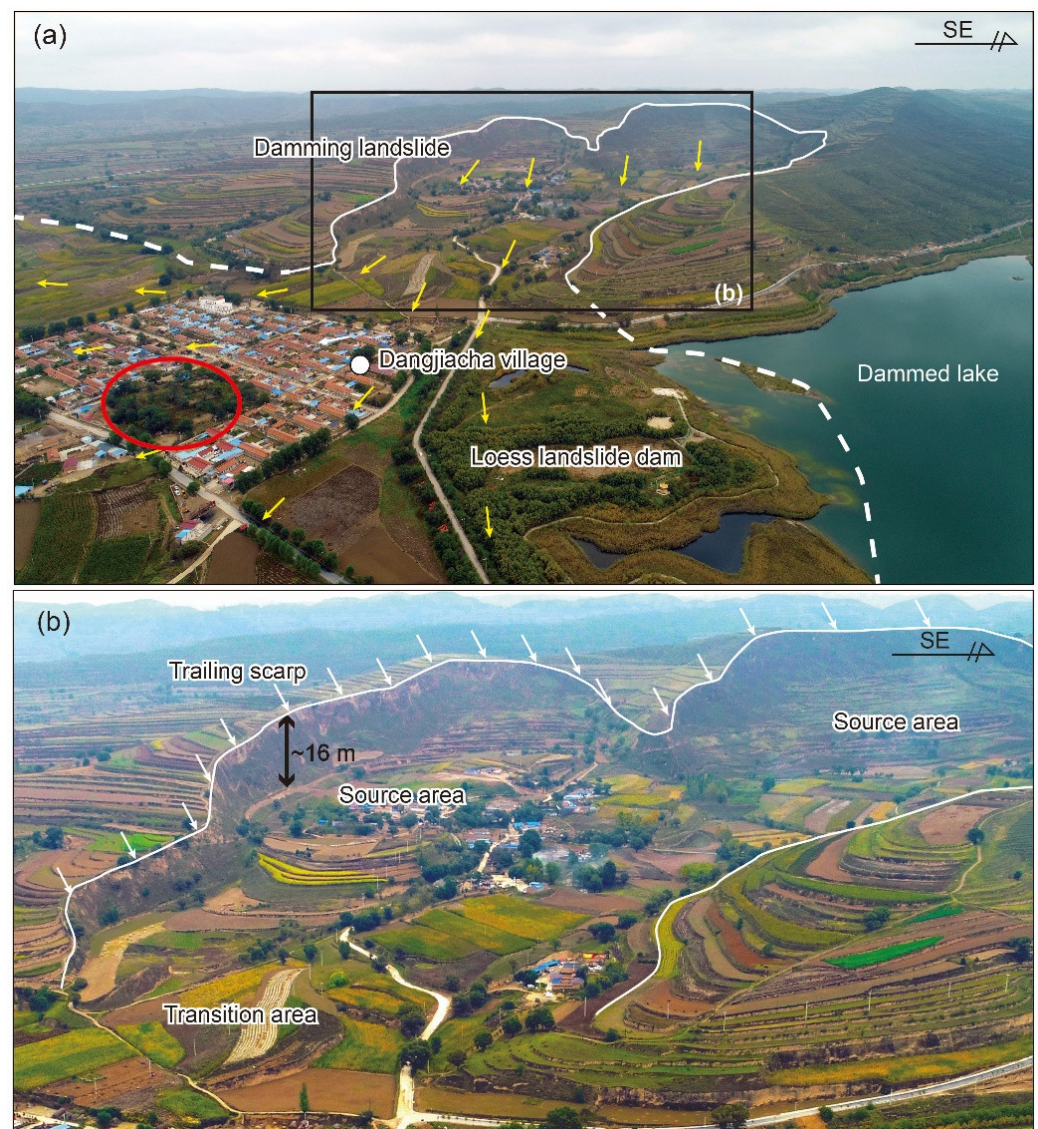


Figure 3. Field photograph of Haiyuan-earthquake-triggered landslide at Dangjiacha village ($35.841205^{\circ}\text{N}$, $105.462299^{\circ}\text{E}$). (a) The material loss in the landslide area and the steep trailing scarp are apparent. The position indicated by the red circle shows that the loess landslide dam surface is uneven. (b) The detailed UAV photo shows the source area of the Dangjiacha landslides.



Figure 4. Multi-temporal Google Earth images and UAV survey images. (a–e) Different temporal Google Earth images in the same view; (f) UAV images obtained from field investigation.

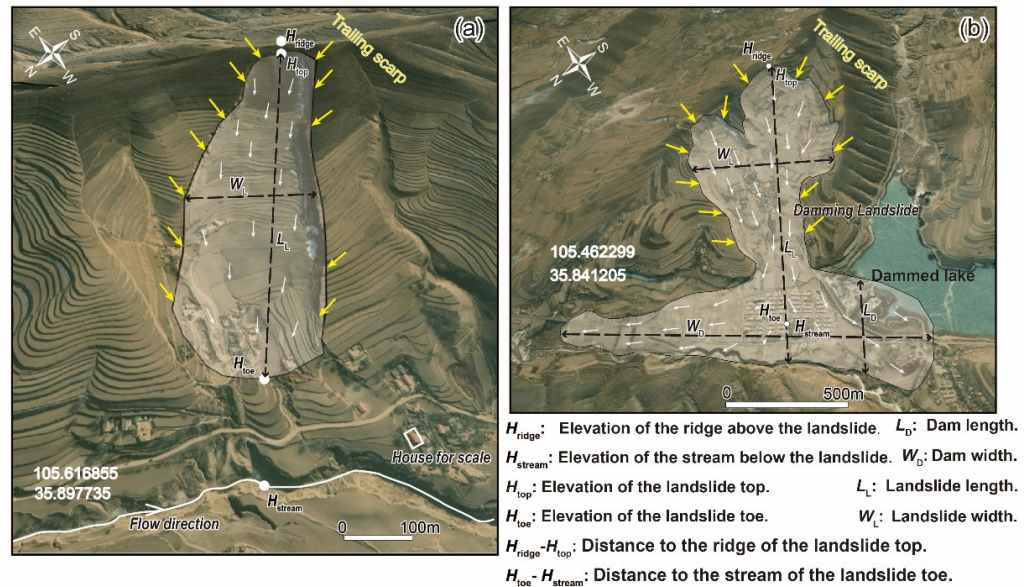


Figure 5. Interpretation principle and the attribute statistics method for (a) non-damming and (b) damming landslides. Yellow arrows depict the locations of the trailing edge and side edge, and white circles depict the locations of altitude values. The arrows indicate the measurement principles of the parameters. Note that we measured the length from the landslide’s top to the toe as the landslide length and the maximum width of the transition area as the landslide width.

Previous studies have reported that the spatial distribution of earthquake-triggered landslides is mainly affected by seismic, terrain, and geological factors [43–48]. In this study, we selected elevation, relief, slope, aspect, and distance to rivers as terrain factors; strata and loess thickness as geological factors; and distance to the seismogenic fault (HYF) as a seismic factor [22,30]. The 12.5 m ALOS DEM (<https://search.asf.alaska.edu>, accessed on 2 November 2018) was used to analyze topographic factors, including elevation, slope, aspect, relief, and river locations. All terrain factors were divided into discrete classes at equal intervals within the primary data range of the study area into discrete classes (Table 1, Figure 6a–e). Strata data were obtained from a 1:200,000 geological map (<http://dcc.ngac.org.cn/geologicalData/cn/geologicalData/details/doi/10.23650/data.A.2019.NGA120157.K1.1.1.V1>, accessed on 2 May 2021), which were divided into 6 categories according to the stratigraphic age groups, including Holocene (Q_h), Pleistocene (Q_p), Neogene (N), Paleogene (E), Pre-Paleogene (Pre-E), and Magmatite. The loess thickness was obtained from previous studies [30,49], which was divided into 7 categories with 50 m intervals (Table 1, Figure 6f). The HYF was obtained from a 1:4,000,000 scale of the active faults in China [42]. The study area was divided into 7 categories according to their distance to the HYF (Table 1, Figure 6f).

Table 1. Classification of the terrain, geology, and seismic factors used in the spatial distribution analysis.

	Factors	Classification
Terrain	Elevation (m)	(1) <1500, (2) 1500–1700, (3) 1700–1900, (4) 1900–2100, (5) 2100–2300, (6) 2300–2500, (7) >2500.
	Relief (m)	(1) <200, (2) 200–400, (3) 400–600, (4) 600–800, (5) 800–1000, (6) 1000–1200.
	Slope (°)	(1) <5, (2) 5–10, (3) 10–15, (4) 15–20, (5) 20–25, (6) 25–30, (7) 30–35, (8) 35–40, (9) 40–45, (10) 45–50, (11) >50.
	Aspect	(1) Flat, (2) N, (3) NE, (4) E, (5) SE, (6) S, (7) SW, (8) W, (9) NW.
	Distance to rivers (km)	(1) <1, (2) 1–2, (3) 2–3, (4) 3–4, (5) 4–5, (6) 5–6, (7) 6–7.
Geology	Loess thickness (m)	(1) 0, (2) 0–50, (3) 50–100, (4) 100–150, (5) 150–200, (6) 200–250, (7) >250.
	Strata	(1) Q_h , (2) Q_p , (3) N, (4) E, (5) Pre-E, (6) Magmatite.
Seismic	Distance to HYF (km)	(1) <10, (2) 10–20, (3) 20–30, (4) 30–40, (5) 40–50, (6) 50–60, (7) 60–160.

In this study, we converted all factors data into raster form, with a grid cell size of 12.5 m × 12.5 m to perform a spatial distribution analysis (Figure 6).

3.2. Spatial Distribution Analysis of Damming Landslides

The background area and the total, damming, and non-damming landslides present in each class of every factor were calculated using the spatial statistics tool in ArcGIS. Then, the proportion of damming landslide area to the total landslide area in each classification (PCDL) and the proportion of the total damming landslide area to the total landslide area (PTDL) were calculated. Abnormal distribution factors were identified by comparing the PCDL and the PTDL.

$$PCDL = \frac{\text{damming landslide area in one classification}}{\text{all landslides area in the corresponding classification}} \times 100\% \quad (1)$$

$$PTDL = \frac{\text{total damming landslides area}}{\text{all landslides area}} \times 100\% \quad (2)$$

Moreover, to explore the main controlling factors of the damming landslide distribution, we evaluated the importance of the eight factors affecting the spatial distribution of damming and non-damming landslides using the information gain (IG) function. IG is a rapid and easily implemented factor-ranking method. Information gain (IG) is also

referred to as mutual information, representing the expected reduction in H (where entropy, H , is the measure of disorder) produced by partitioning the dataset according to a given attribute. The IG for an outcome Y from an attribute X represents the expected decrease in the entropy of Y conditioned on X . The more information the factor provides regarding the landslide distribution, the higher the IG value [45]. The specific formula is as follows:

$$IG(Y, X) = H(Y) - H(Y|X) \quad (3)$$

where $H(Y)$ represents the entropy of Y , and $H(Y|X)$ represents the entropy of Y given X . $H(Y)$ can be written as

$$H(Y) = - \sum_{i \in 1}^k p_i \log_2 p_i \quad (4)$$

where p_i represents the proportion of instances belonging to class i in the data.

$H(Y|X)$ can be written as

$$H(Y|X) = \sum_{j \in X}^j p_j H(Y|X = j) \quad (5)$$

where p_j represents the probability that attribute X takes on value j in the data; thus:

$$H(Y|X = j) = \sum_{i \in 1}^k p_{(i|j)} \log_2 p_{(i|j)} \quad (6)$$

To calculate IG , we randomly selected 7834 sampling points within the landslide zone (65 were located within the damming landslide area) and 7834 sampling points outside the landslide area. We extracted and ranked the IG values of all eight factors for the sample points of damming, non-damming, and total landslides. An example calculation of IG is provided in the Supplementary Materials.

3.3. Morphometry Analysis of Damming Landslides

The morphometry of the damming landslides and all HYEQ-triggered landslides, including the aspect ratio (landslide length/width ratio), landslide area, and equivalent coefficients of friction (landslide height/travel distance (landslide length) ratio), were displayed in a probability density diagram. The probability density diagram can intuitively reflect the scale and distribution of the landslide, which can be used to compare the differences between “damming landslides” and “all landslides” to highlight the specific characteristics of the former category. Furthermore, we calculated the trends of landslides based on the parameters of H_{top} , H_{toe} , H_{ridge} , and H_{stream} (Figure 5). The landslide position was normalized to the total height of the slope. The distance from the landslide top to the ridge (d_{rid}) and the toe to the stream (d_{st}) can be expressed as $\left| \begin{matrix} d_{\text{rid}} \\ d_{\text{st}} \end{matrix} \right| = (H_{\text{ridge}} - H_{\text{top}}), (H_{\text{toe}} - H_{\text{stream}}) / (H_{\text{ridge}} - H_{\text{stream}})$ [30]. We projected all the d_{rid} and d_{st} in a rectangular coordination system.

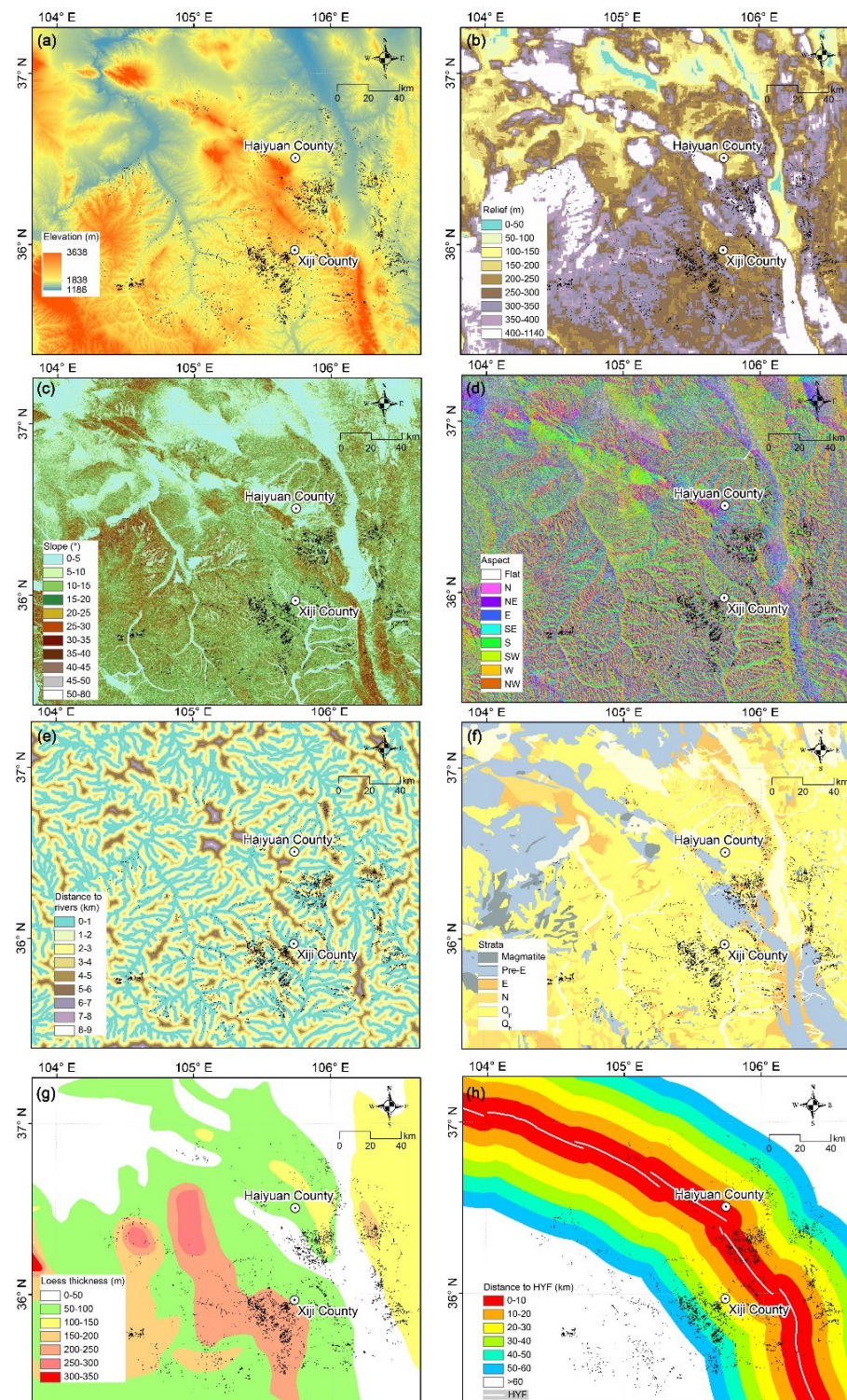


Figure 6. Factor maps used in analyzing the spatial distribution of damming landslides. Terrain factors: (a) elevation, (b) relief, (c) slope, (d) aspect, and (e) distance to rivers. Geological factors: (f) strata and (g) loess thickness. (h) Earthquake factor: distance to HYF. Terrace data were extracted from ALOS DEM (<https://search.asf.alaska.edu>, accessed on 2 November 2018). Strata data were obtained from a 1:200,000 geological map (<http://dcc.ngac.org.cn/geologicalData/cn/geologicalData/details/doi/10.23650/data.A.2019.NGA120157.K1.1.1.V1>, accessed on 2 May 2021). Location of HYF referred 1:4,000,000 scale of the active fault in China [42].

4. Results

4.1. Survey of Damming Landslides

A total of 65 damming landslides were identified from the HYEQ-triggered landslide inventory [20,21]. The area of total damming landslides is $1.84 \times 10^7 \text{ m}^2$, and the average is $2.8 \times 10^5 \text{ m}^2$. More than 80% of these were concentrated in western Xiji County (Figure 7). The rest were observed in the western front of Liupanshan Mountain (Figure 1c). Several important LDLKs were distributed along the Hongzhuang River (Landslides _2, _3, _5, and _6 in Figure 7). Landslide_2 dammed the largest LDLK, with an area of $1.1 \times 10^6 \text{ m}^2$. The average area of the LDLKs is $\sim 2.0 \times 10^5 \text{ m}^2$, and the smallest is $\sim 4.4 \times 10^3 \text{ m}^2$. Its catchment area was also the largest, at approximately $9.6 \times 10^7 \text{ m}^2$. The catchment areas of other damming landslides in tributaries are small. The average is $1.2 \times 10^7 \text{ m}^2$, and the smallest is approximately $8.9 \times 10^5 \text{ m}^2$. It was assumed that the thickness of the landslide was equal everywhere. The landslide volumes of 89 well-preserved HYEQ-triggered landslides were calculated based on each landslide's area and the mean thickness obtained from predecessors' field investigations [30]. According to the power-law relationship between the area and volume of the landslides triggered by the HYEQ, $V = 4.17 \times A^{1.086}$ [30], the volume of the damming landslides ranges from $1.2 \times 10^5 \text{ m}^3$ to $1.8 \times 10^7 \text{ m}^3$ (more details are provided in the Supplementary Materials).

4.2. Features of Representative Damming Landslides

We selected three representative damming landslides in which the landslide dams were well-reserved, abandoned, and artificially modified, respectively, for a detailed description (Landslide_2, Landslide_42, and Landslide_31 in Figure 7).

Landslide_2 is located on the side of the trunk stream of Hongzhuang River, of which the dam is well-reserved (Figure 7). The area of Landslide_2 is approximately $1.3 \times 10^6 \text{ m}^2$, with a length of approximately 2180 m and a width of approximately 680 m. The trailing edge and side edge form cliffs in a semi-circular arc, similar to a chair back (Figure 8a,b). Its transition and accumulation areas (approximately 80% of the affected area) are flat compared with the surrounding areas. There is no discernable boundary between the transition and accumulation areas (Figure 8h,i). The material flows and fills the downstream and upstream of the valley with a low thickness (approximately 16 m) (Figure 8g). The landslide dam has the shape of a flat strip. Its length is consistent with the width of the valley (approximately 320 m). Its width (approximately 1.4 km) is approximately four times its length (Figure 8g–i).

Landslide_42 is located on the tributaries of the Hongzhuang River, of which the dam is abandoned (Figure 7). Its area is approximately $5.7 \times 10^5 \text{ m}^2$, with an approximate length of 1550 m and an approximate width of 420 m (Figure 8c,d). The upstream area of the landslide dam comprises the flat lake deposition, and the downstream area contains a deep valley. Landslide_42's accumulations were damaged (Figure 8j), and the LDLKs dried up, leaving sporadic ponds. The continuous headward erosion of the deep downstream channel made it challenging to identify the original accumulation areas. We inferred from the topographic profile that the length, width, and height of the original Landslide_42 dam were approximately 370 m, 470 m, and 18 m, respectively (Figure 8j,k).

Landslide_31 is located on the side of a small valley mouth, of which the dam has been artificially reconstructed. Its area is approximately $2.6 \times 10^5 \text{ m}^2$, with an approximate length of 920 m and an approximate width of 310 m (Figure 8e,f); the natural dam height is approximately 7 m (Figure 8l). It partially blocked the valley (Figure 8m). An artificial dam was built based on the landslide dam. After this modification, the dam was approximately 20 m high. A flat lake deposition was formed upstream of the artificial dam (Figure 8f,l).

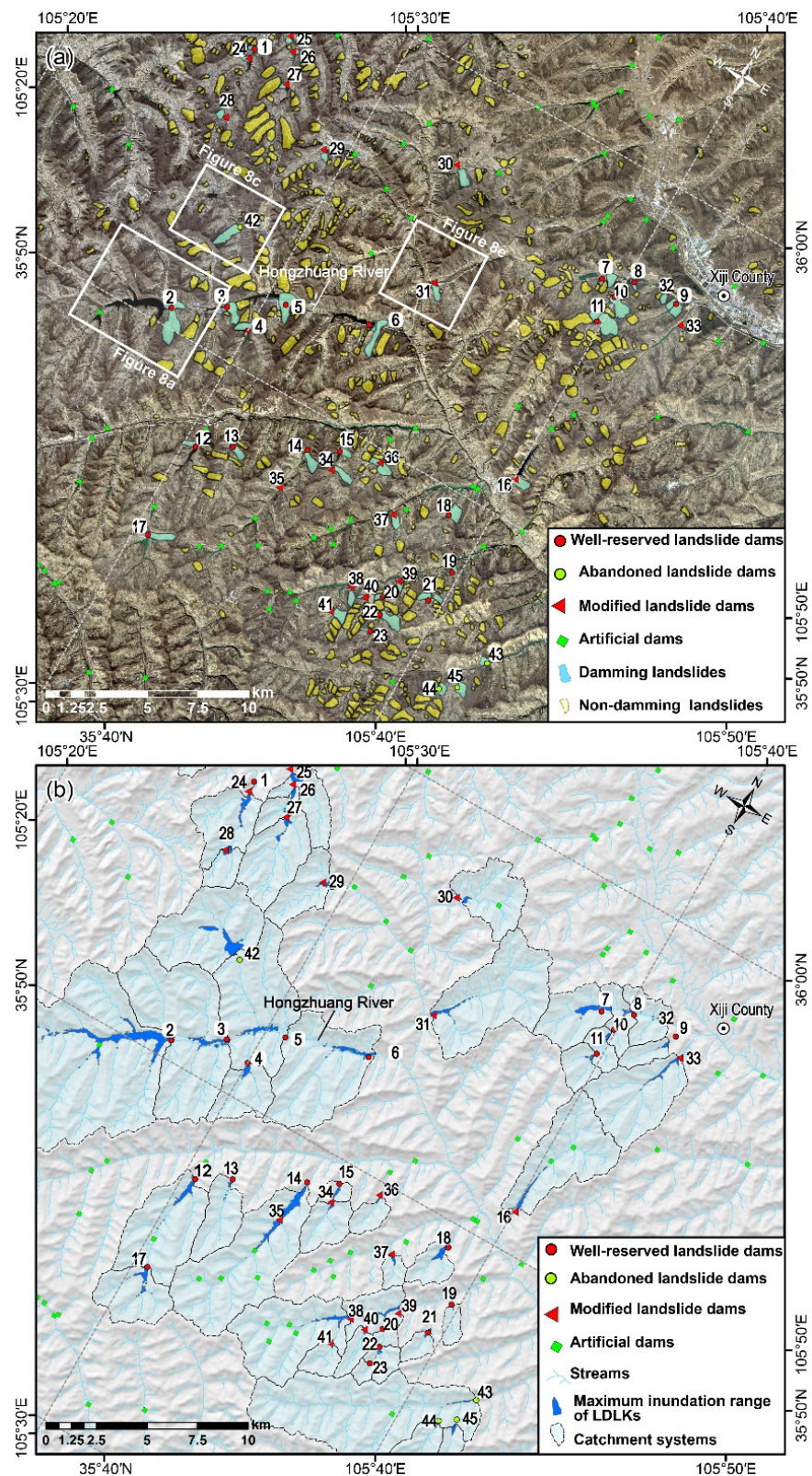


Figure 7. Distribution of landslides and landslide dams in western Xiji County [21]. (a) The background is derived from GF-1 images. Damming landslides and non-damming landslides are shown in yellow and cyan, respectively. (b) The background is derived from hillshade images. The figure shows the stream network, watershed, and the inundation range of LDLKs.

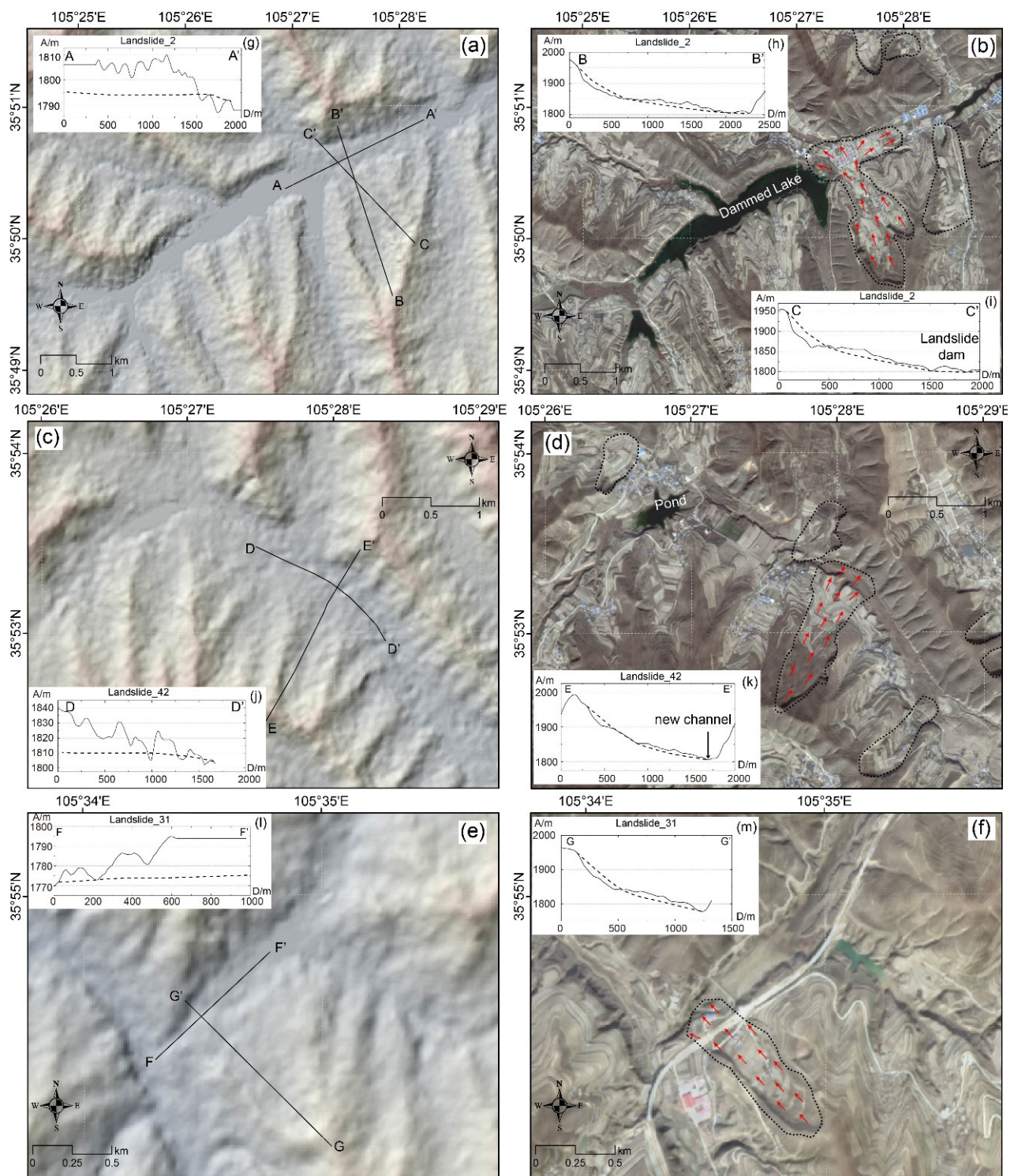


Figure 8. GF-1 Images and ALOS DEM showing the representative damming landslides. (a,b) Damming landslide of which the dam is well-reserved (Landslide_2 in Figure 7). (c,d) Damming landslide of which the dam is abandoned (Landslide_42 in Figure 7). (e,f) Damming landslide of which the dam has been artificially modified (Landslide_31 in Figure 7). (g–i) Thick dashed lines in the profiles denote the possible previous surface prior to the Landslide_2. (j,k) Thick dashed lines in the profiles denote the possible previous surface prior to the Landslide_42. (l,m) Thick dashed lines in the profiles denote the possible previous surface prior to the Landslide_31. The red arrows show the direction of movement.

4.3. Spatial Analysis of Damming Landslide Distribution

The damming landslide area, non-damming landslide area, background area, *PCDL*, and *PTDL* in each classification of the controlling factors are illustrated in Figure 9. We detailed this information in the order of terrain, geological, and seismic factors, and calculated each variable's *IG* information.

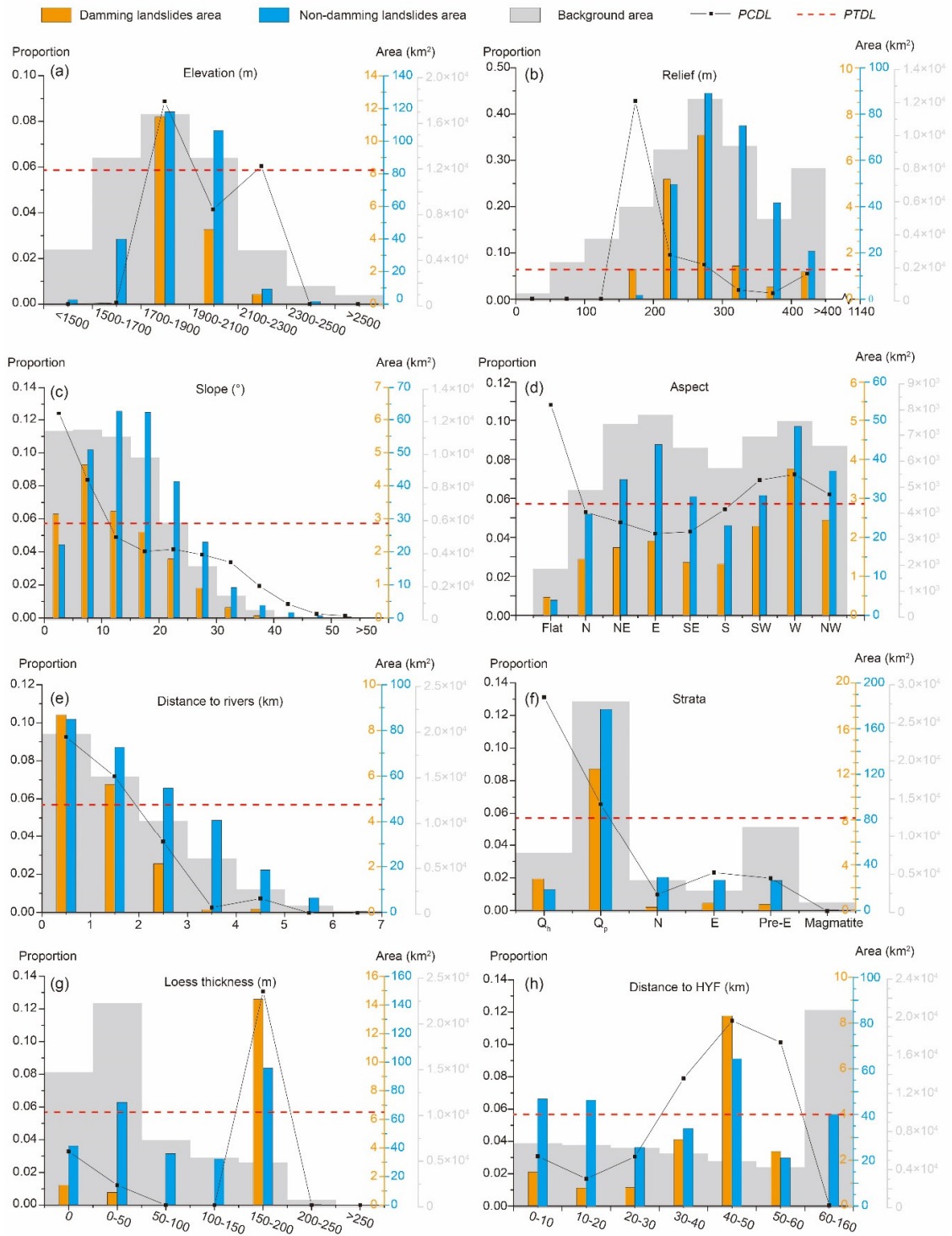


Figure 9. Histogram of the classified area of coseismic damming landslides and non-damming landslides. (a) Elevation, (b) relief, (c) slope, (d) aspect, (e) distance to rivers, (f) strata, (g) loess thickness, and (h) distance to HYF.

4.3.1. Terrain Factors of Damming Landslides

For this study, we selected terrain factors, including elevation, relief, slope, aspect, and distance to rivers for analysis. The elevations of the damming landslides ranged between 1700 and 2300 m, and the *PCDL* was slightly larger than the *PTDL* at 1700–1900 m and slightly smaller than the *PTDL* at 1900–2100 m (Figure 9a). For the terrain relief variable, the damming landslides were distributed within 150 and 400 m. The *PCDL* was much higher than the *PTDL* in the 150–200 m range and much lower than the *PTDL* in the range of 300–400 m, indicating that the damming landslides were concentrated in areas with a low relief (Figure 9b). The area distribution of the classified slope for damming landslides shows a typical distribution pattern in the range of 0° – 40° and a peak of 5° – 10° . The distribution of non-damming landslides showed a typical distribution pattern, with a peak of 10° – 20° . The *PCDL* was much higher than the *PTDL* in the classification of 0° – 5° and much lower than the *PTDL* at 15° – 45° ; this means that the slope within the damming landslide area was smaller (Figure 9c). Regarding the slope aspect, the *PCDLs* of all classifications were almost close to the *PTDL*, except for the flat direction. The *PCDL* was much higher than the *PTDL* for the flat category (Figure 9d). The damming, non-damming landslide area, and the *PCDL* decreased with increasing distance from the river. The *PCDL* was larger than the *PTDL* within 2 km and smaller than the *PTDL* over 2 km. The decreasing trend of the *PCDL* indicates that the damming landslides were close to rivers (Figure 9e).

4.3.2. Geological Factors of Damming Landslides

The damming landslides fell within the stratigraphic distribution range of the Holocene (Q_h) and Pleistocene (Q_p). Most were distributed in the strata of the Pleistocene. Few were distributed in the strata before the Quaternary (N, E, Pre-E, and Magmatite). However, the *PCDL* was only higher than the *PTDL* in the Holocene strata distribution zone. In the Pleistocene strata distribution zone, the *PCDL* was consistent with the *PTDL* (Figure 9f). The lithology of the Pleistocene strata in the study area was loess [50]. To further detail the distribution characteristics in LP, we determined the relationship between the loess thickness and landslides (Figure 9g). The loess thickness in the study area varied from a few meters to approximately 300 m [30]. The damming landslides were concentrated in the area with a loess thickness of 150–200 m. Meanwhile, in this area, the *PCDL* was larger than the *PTDL*.

4.3.3. Seismic Factors of Damming Landslides

The distance from the landslide to the HYF was deemed to be a seismic factor (Figure 9h). Damming landslides were distributed within 60 km of the HYF. There was no apparent correlation between the distribution of damming landslides and the distance to the fault. The *PCDL* of damming landslides was larger than the *PTDL* in the range of 30–60 km away from the fault, and the most significant *PCDL* appeared in the range of 40–50 km.

4.3.4. Importance Ranking of the Controlling Factors

The value of *IG* reflects the importance of control factors for landslide damming [45]. The ranking of the importance the obtained control factors, in descending order on the basis of *IG*, is shown in Table 2, and all eight control factors are listed in descending order by weight. The orders of the factors contributing to all landslides and non-damming landslides were almost the same, and the first three factors were relief, distance to the fault, and slope, which correspond to the importance rankings of earthquake-triggered landslides [45,51]. The ranking of the loess thickness was the highest for damming landslides, which was considerably different from all landslides and non-damming landslides. This means that loess thickness was the most critical factor affecting the distribution of damming landslides.

Table 2. Ranking of *IG* values.

Ranking	Damming Landslides		Non-Damming Landslides		All Landslides	
1.	Loess thickness	0.007845	Relief	0.133636	Relief	0.131218
2.	Distance to fault	0.004142	Slope	0.075333	Distance to fault	0.071287
3.	Slope	0.002112	Distance to fault	0.072278	Elevation	0.069379
4.	Elevation	0.002104	Elevation	0.071701	Slope	0.067805
5.	Relief	0.002074	Strata	0.053099	Strata	0.049012
6.	Strata	0.001515	Loess thickness	0.044867	Loess thickness	0.041564
7.	Distance to river	0.000942	Aspect	0.027055	Aspect	0.02316
8.	Aspect	0.000268	Distance to river	0.003304	Distance to river	0.00002

4.4. Morphometry of Damming Landslides

We calculated the morphometry of the damming landslides and total landslides and displayed the data using a probability density curve (Figure 10). For the aspect ratio (L/W), the probability density curve of damming landslides primarily ranged from 0.375 to 3.375, with peaks ranging from 0.875 to 2.5. In contrast, all landslides primarily ranged from 0.375 to 2.125, with a single peak of 0.875 (Figure 10a). This suggests that the predominant shape of all landslides was close to a square, with a similar length and width. On the other hand, for the damming landslides, rectangular landslides with a length and width ratio of approximately two also accounted for a high proportion.

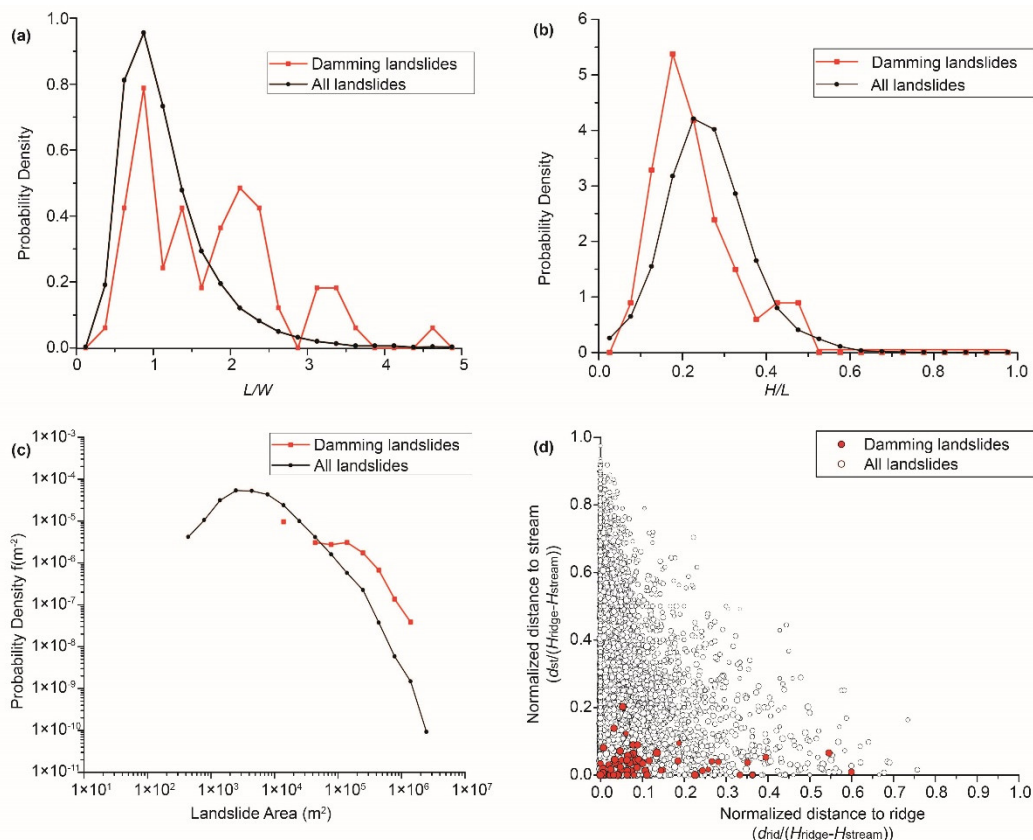


Figure 10. Geomorphic attributes of the Haiyuan coseismic damming and non-damming landslides (landslide data after Xu et al., 2021) [21]. (a) Aspect ratios of landslides. (b) Equivalent coefficients of friction. (c) Areas of landslides. (d) Normalized distances to ridges and streams, revealing the coseismic landslide distribution in slope portions. The horizontal axis is the normalized distance of the landslide boundary to the top of the slope (the ridge). The vertical axis is the normalized distance to the bottom of the slope (the river valley).

For the equivalent coefficient of friction (H/L), the probability densities curve of the damming landslides ranged from 0.025 to 0.475 with a peak of 0.2, whereas all landslides primarily ranged from 0.025 to 0.725 with a peak of 0.25. The damming landslides moved greater distances than all landslides given an equivalent slope height. This indicates that the travel distances of damming landslides were much longer than others in the group of all landslides (Figure 10b).

For the landslide area, the probability densities of the damming landslides ranged from $1.4 \times 10^4 \text{ m}^2$ to $1.4 \times 10^6 \text{ m}^2$, whereas all landslides ranged from $4.4 \times 10^2 \text{ m}^2$ to $2.5 \times 10^6 \text{ m}^2$. The probability densities of damming landslides were higher than those of all landslides (Figure 10c), which means that the damming landslides exhibited large areas among all landslides.

Another attribute is the landslide position on the slope, as shown in Figure 10d. The horizontal axis represents the normalized distance from the landslide top to the slope top (ridge). The vertical axis represents the normalized distance from the landslide toe to the slope bottom (stream). Almost all damming landslide markers were close to the axes, indicating that most damming landslides slid from the slope's top to bottom.

In conclusion, damming landslides typically slid from the top to the bottom of the slope. Landslides with large scales and long sliding distances were more likely to block valleys in the LP. Most damming landslides presented a square to a rectangular shape, with an aspect ratio of 0.875–2.5.

5. Discussion

5.1. Characteristic Comparison between Damming and Non-Damming Landslides in the LP

Damming landslides can be easily interpreted based on their large volume and topographical transformation using the coseismic landslides inventory. The damming landslides in this study were selected according to the abovementioned principles regarding damming landslides. The landslide dams reported in previous studies have primarily occurred in southwestern Xiji County [21,30], which is consistent with the areas in which the distribution was concentrated in this study. The number of landslides in this study was also close to the totals found in previous research [21,30]. Therefore, the damming landslide inventory contains most of the HYEQ-triggered damming landslides.

The abnormal distribution characteristics of damming landslides include lower terrain relief, slower slope, closer proximity to the river, a higher proportion of flat aspects, and a higher loess thickness than those of non-damming landslides in the LP. Because the DEM data were collected within the past ten years, the terrain factors calculated using the DEM may have been influenced by the landslide reconstruction process. It is therefore necessary to determine the abnormal terrain factors that existed before landslide reconstruction, as well as those that were caused by landslide reconstruction. These factors were determined by comparing the original resolution of the factors with the landslide length. If the resolution of the factor was smaller than the landslide length, the controlling factors were affected; otherwise, they were not affected. The average length and width of all HYEQ-triggered landslides was 181 m and 165 m, respectively; therefore, landslide reconstruction can affect the factors of slope and aspect (with a resolution of 12.5 m). The landslide transformation did not affect the relief (resolution is 1125 m), the distance to the river (1000 m), or the loess thickness (larger than 1000 m). The abnormal geometric characteristics of the damming landslides include a large L/W , low H/L , large area, and entire slope failure.

The abnormal characteristics of damming landslides are consistent with their mechanism, which may be jointly affected by the site effect of loess [52] and its flow liquefaction [34,35]. The site effect of the deposit thickness and topography of loess sites in the LP of China on ground motion amplifies the peak ground acceleration. This extended the predominant periods of ground motion [52]. Therefore, the initial sliding position of the loess landslide in the HYEQ is near the ridge (Figure 10d) and accounts for a high proportion of the area with a high loess thickness [33] (Figure 9g), which is also significant for the distribution of damming landslides. Landslides influenced by the loess liquefaction

effect are characterized by a high mobility and a long runout distance, even along a very gently sloping travel path [34]. These characteristics can be reflected by an apparent friction (H/L) value of less than 0.2 [53]. Most landslides on the loess tableland with long runout distances show their geometry of strips and banding. In this study, the H/L curve peak of the damming landslides (approximately 0.2) was smaller than that of all landslides (approximately 0.25). This means that loess liquefaction was more likely to influence damming landslides. Other abnormal characteristics of damming landslides included large scales, large L/W , and the gentle slope, which were also influenced by the loess liquefaction flow [34]. Due to the loess flow, the HYEQ-triggered loess landslide material can travel a long way from the tributary ditch to the main river and block the main river (such as the Landslide_6, shown in Figure 7). Some landslide dams have a width that is much larger than the length, which is also formed by landslide materials flowing a long distance along the valley (Figure 3).

Damming landslides were distributed more closely to the main river. These slope failures require a large volume and long-runout distance, as well as a large catchment area to form LDLKs. Some landslides located upstream of the branch ditch were far away from the main river and blocked the valley. However, they could not form LDLKs because of the small catchment area.

In conclusion, the characteristics of damming landslides in LP include: (1) large L/W values, primarily larger than two, (2) a small H/L , mostly less than 0.2, (3) a large scale ($>10^5 \text{ m}^2$), (4) a gentle slope in the landslide area, and (5) a more substantial proportion within thick loess distribution areas.

We have demonstrated the characteristics of damming and non-damming landslides observed in the LP in this study using a cartoon model (Figure 11). For damming landslides, the materials flow easily, as they are displaced out of the source area after long-distance transport, and it is easy to block the river under these. Most of these landslides occurred in areas with thick loess, close to the river. In contrast, non-damming landslide material was deposited near the source area.

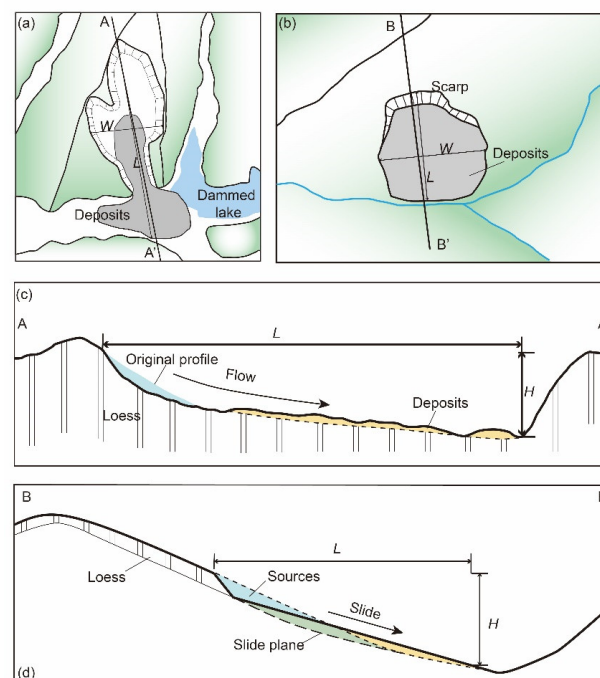


Figure 11. Models of damming and non-damming landslides. (a) Plane distribution of a damming landslide. (b) Plane distribution of a non-damming landslide. (c) Geological section of a damming landslide; profile location in (a). (d) Geological section of non-damming landslide; profile location in (b).

5.2. Comparison of Characteristics of Landslide Dams in the LP and the Global Database

Landslide dams are an important part of damming landslides. In this study, we compared the landslide dams in the LP with other landslide dams to highlight the characteristics of landslide dams in the LP, which is helpful in exploring the role of damming landslides in the evolution of the regional topography. It also provides a reference for the treatment of damming landslides.

Fan et al. (2020) have summarized the global landslide dam database, which contains >1800 landslide dams compiled from literature data [10]. In this study we tried to collect the complete variables for each damming landslide. The data in this study supplement the global inventory and highlight the characteristics of loess landslide dams [10].

The morphometry of landslide dams reflects the movement of river blockages. We classified landslide dams according to the widely accepted geomorphometric classification method developed by Costa and Schuster (1988) [54]. This method classifies landslide dams based on the relationship between their shape and size and the blocked valley [10,54]. Type I dams are dams that partially block a river. Type II dams are dams that totally block a river. Type III dams are dams that do not only block a river and of which the accumulated materials are distributed both upstream and downstream. Type IV dams are dams that are formed from the contemporary movement of two or more landslides detached from opposite sides of the same valley. The 65 damming landslides caused a total of 54 landslide dams, including 22 of Type I dams, 17 of Type II dams, 5 of Type III dams, and 10 of Type IV dams (Table 3). The proportion of Type I landslide dams triggered by the HYEQ was higher than that in the global database, and that of Type III was lower [10]. However, the best-preserved landslide dams along the Hongzhuang River were Type III dams.

Table 3. Geomorphometric loess landslide dam classifications.

Types [54]	Amount	Features	Ratio (%)
I	22	Landslide dams partially blocking the river	41
II	17	Landslide dams totally blocking the river	31
III	5	Landslide dams filling the valley from side to side, and with accumulated materials distributed both upstream and downstream of the release area	9
IV	10	Contemporary movement of two landslides detached from opposite sides of the same valley	19

Stability is the most important characteristic of loess landslide dams and they can persist for over a century. The dimensionless blockage index (DBI) is the best geomorphic stability index [10]. We calculated the DBI of the loess landslide dams using $DBI = \log(A_C \times H_D/V_D)$. The maximum DBI in this study was approximately 2.65, which was much less than the upper boundary of stable dams from the global inventory, approximately $DBI = 2.75$ [7]. Therefore, landslide dams in the LP were more stable than those in most cases worldwide.

Compared with the rock damming landslides, such as damming landslides triggered by the 2008 Wenchuan earthquake [13,14,55–57], the type of loess damming landslides was single, which primarily consists of loess flows [14,28]. The loess landslide dam height and catchment area were smaller, and the loess landslides were distributed in a flatter area (slope < 35°) and trend with regard to the entire slope failure.

5.3. Landscape Implications of Damming Landslides in LP

Landslides aggravated casualties during the HYEQ [21]. However, the long-term impacts of damming landslides in LP have been positive. Long-existing dams can control intermontane sedimentation and denudation [10], which is evident in the LP with intense erosion [58]. Landslide dams play an essential role in conserving regional water and

sediment. Some narrow valley branches have silted, resulting in upstream flat farmland; one such example includes Landslide_42 (Figure 7).

Some LDLKs have existed throughout the years, with a large catchment area in the arid study area (the average annual precipitation is less than 400 mm and the annual evapotranspiration is approximately 1500 mm) [34] (Figure 7). This phenomenon may be related to the shallow depth of groundwater [34]. Water in the LDLKs can be continuously exchanged with the shallow groundwater. The shallow lake (no more than the dam height) and sediment silting make it challenging to form destructive stress on a long and thin dam body. The permanent lake in the narrow valley has improved the local climate and the living environment. The regional topography has evolved to a slower slope and a lower relief, which benefits agricultural development and human survival in drought in the LP. The dammed lake provides water for residents' living requirements and irrigation. With slight reconstruction, local people can build houses and canals for living and farming on the original loess landslide dams (Figure 12). In addition, damming lakes have become a tourist attraction that has driven the local economy, and the village is known as a town with earthquake lakes (earthquake-triggered dammed lakes). The loess dam has positively impacted the reconstruction of the terrain over a long period. As a result, several artificial dams have been constructed in this area (Figure 7).

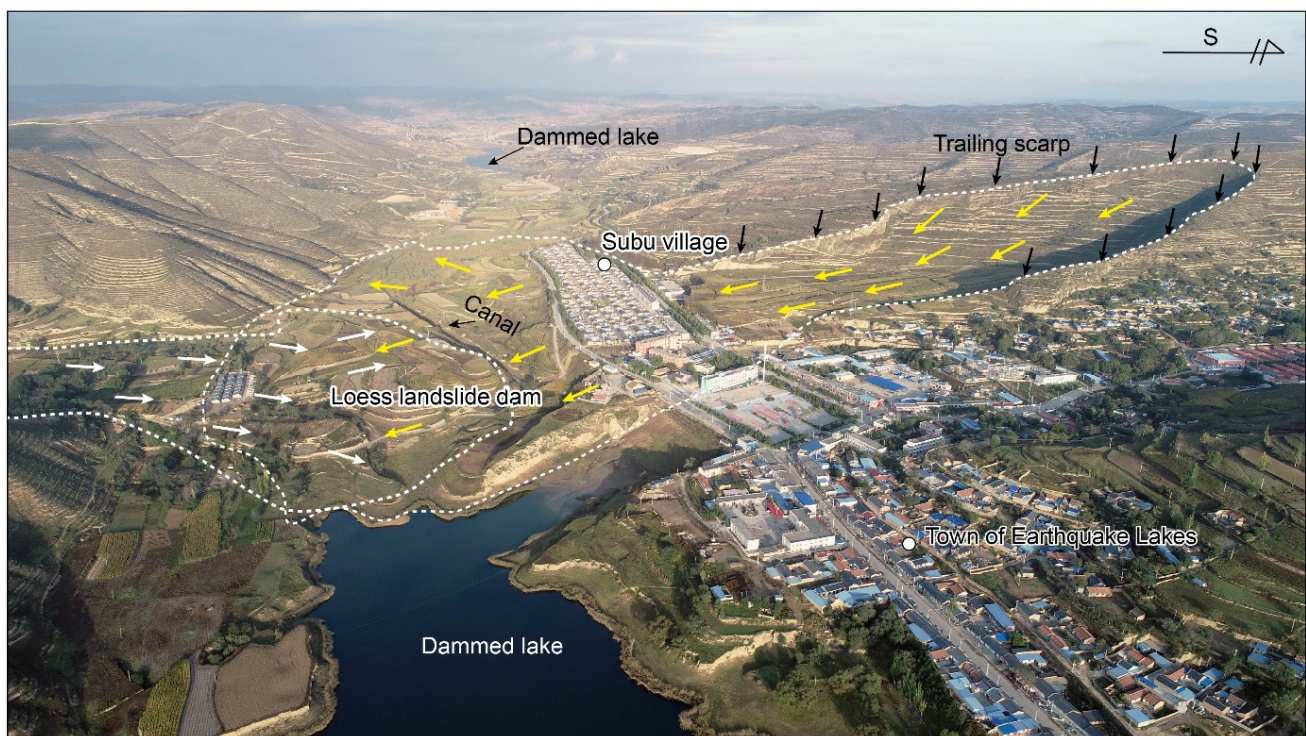


Figure 12. Damming landslide at Subao village (No. 5 landslide dam in Figure 7). The loess landslide dam surface is uneven. Local people build houses and canals on the loess landslide dam for living and farming on the original landslide dam with slight reconstruction measures.

5.4. Deficiencies and Prospects

In this study, we provide an earthquake-triggered landslide dam inventory around Xiji City, along with preliminary analyses of their spatial distribution, morphometry, and landscape evolution. This provides essential data and inspiration for susceptibility analyses and risk predictions of future landslide dams in the LP, as well as updating the worldwide landslide dam database.

Notably, the analysis in this study also has some limitations. First, the controlling factors used to analyze the damming landslide distribution are mainly topographic factors, whereas seismic and hydrological factors are neglected. Second, the stability analysis

of landslide dams in this study was based on morphological features, but we neglected the dam composition and loess structure. Another limitation is that in this study we did not quantify the terrestrial sediment flux and sediment budget, which are essential in the landscape evolution of loess landslide dams.

6. Conclusions

We established an inventory of 65 damming landslides and 54 landslide dams triggered by the 1920 $M\sim 8.0$ Haiyuan earthquake, which were identified via visual interpretation. Their controlling factors and morphometry were determined and analyzed in detail. The main conclusions are as follows.

(1) The distribution of damming landslides triggered by the Haiyuan earthquake is concentrated. More than 80% of the damming landslides were found to be concentrated in western Xiji County.

(2) The damming landslides were distributed in areas closer to rivers than not, with a high loess thickness and low relief. Influenced by the loess liquefaction flow, the slopes where the damming landslides were located were gentle. The geometric characteristics of damming landslides include a large aspect ratio (L/W), low equivalent coefficients of friction (H/L), large scales, and entire-slope failure.

(3) Loess thickness was the most critical controlling factor of the Haiyuan earthquake-triggered damming landslide distribution.

(4) Loess landslide dams are stable and can be reformed to reservoir dams, which assist in conserving water and sediment in upstream areas. Therefore, it is beneficial in the long term to flatten the upstream area, as this would cause the regional topography to evolve into a slower slope and lower relief.

Supplementary Materials: The following supporting information can be downloaded at: <https://www.mdpi.com/article/10.3390/rs14102427/s1>, Method of how Information Gain (IG) works in detail and the datasets of landslide dam and damming landslides used in the manuscript in ArcGIS shp file.

Author Contributions: Conceptualization, Y.X., W.Z. and X.G.; methodology, W.Z., Y.X., P.D., W.L. and X.G.; writing—original draft preparation, W.Z., X.G. and Y.X.; writing, review, and editing, Y.X., Q.T. and W.Z. All authors have read and agreed to the published version of the manuscript.

Funding: This work was supported by the National Natural Science Foundation of China (Grant Nos. 42072248 and 42041006), the National Key Research and Development Program of China (Grant Nos. 2019YFE0108900 and 2021YFC3000601-3) and Scientific Research Project of China Datang Corporation Ltd. (Grant No. DTXZ-02-2021).

Conflicts of Interest: The authors declare no conflict of interest.

References

1. Tacconi, S.C.; Catani, F.; Casagli, N. Geomorphological investigations on landslide dams. *Geoenviron. Disasters* **2015**, *2*, 21. [[CrossRef](#)]
2. Delaney, K.B.; Evans, S.G. The 2000 Yigong landslide (Tibetan plateau), rockslide-dammed lake and outburst flood: Review, remote sensing analysis, and process modeling. *Geomorphology* **2015**, *246*, 377–393. [[CrossRef](#)]
3. Zhong, Q.M.; Chen, S.S.; Wang, L.; Shan, Y.B. Back analysis of breaching process of Baige landslide dam. *Landslides* **2020**, *17*, 1681–1692. [[CrossRef](#)]
4. Fan, X.M.; Yang, F.; Subramanian, S.S.; Xu, Q.; Feng, Z.T.; Mavrouli, O.; Peng, M.; Ouyang, C.J.; Jansen, J.D.; Huang, R.Q. Prediction of a multi-hazard chain by an integrated numerical simulation approach: The Baige landslide, Jinsha River, China. *Landslides* **2020**, *17*, 147–164. [[CrossRef](#)]
5. Guo, X.Y.; Guo, Q.; Feng, Z.K. Detecting the vegetation change related to the creep of 2018 Baige landslide in Jinsha river, SE Tibet using spot data. *Front. Earth Sci.* **2021**, *9*, 706998. [[CrossRef](#)]
6. Korup, O. Geomorphometric characteristics of New Zealand landslide dams. *Eng. Geol.* **2004**, *73*, 13–35. [[CrossRef](#)]
7. Ermini, L.; Casagli, N. Prediction of the behaviour of landslide dams using a geomorphological dimensionless index. *Earth Surf. Process. Landf.* **2003**, *28*, 31–47. [[CrossRef](#)]
8. Evans, S.G.; Delaney, K.B.; Hermanns, R.L.; Strom, A.; Scarascia-Mugnozza, G. The Formation and Behaviour of Natural and Artificial Rockslide Dams; Implications for Engineering performance and Hazard Management. In *Natural and Artificial Rockslide Dams*; Lecture Notes in Earth Sciences; Springer: Cham, Switzerland, 2010; pp. 1–75. [[CrossRef](#)]

9. Harrison, L.M.; Dunning, S.A.; Woodward, J.; Davies, T.R.H. Post-rock-avalanche dam outburst flood sedimentation in Ram Creek, Southern Alps, New Zealand. *Geomorphology* **2015**, *241*, 135–144. [[CrossRef](#)]
10. Fan, X.M.; Dufresne, A.; Subramanian, S.S.; Strom, A.; Hermanns, R.; Stefanelli, C.T.; Hewitt, K.; Yunus, A.P.; Dunning, S.; Capra, L.; et al. The formation and impact of landslide dams-state of the art. *Earth-Sci. Rev.* **2020**, *203*, 103116. [[CrossRef](#)]
11. Xu, W.J.; Xu, Q.; Wang, Y.J. The mechanism of high-speed motion and damming of the Tangjiashan landslide. *Eng. Geol.* **2013**, *157*, 8–20. [[CrossRef](#)]
12. Luo, J.; Pei, X.J.; Evans, S.G.; Huang, R.Q. Mechanics of the earthquake-induced Hongshiyuan landslide in the 2014 M_W6.2 Ludian earthquake, Yunnan, China. *Eng. Geol.* **2018**, *251*, 197–213. [[CrossRef](#)]
13. Fan, X.M.; Western, C.J.V.; Xu, Q.; Gorum, T.; Dai, F.C. Analysis of landslide dams induced by the 2008 Wenchuan earthquake. *J. Asian Earth Sci.* **2012**, *57*, 25–37. [[CrossRef](#)]
14. Tang, R.; Fan, X.M.; Scaringi, G.; Xu, Q.; Western, C.J.V.; Ren, J.; Havenith, H.B. Distinctive controls on the distribution of river-damming and non-damming landslides induced by the 2008 Wenchuan earthquake. *Bull. Eng. Geol. Environ.* **2019**, *78*, 4075–4093. [[CrossRef](#)]
15. Wang, Y.; Cui, L.; Zhang, C.; Chen, W.; Xu, Y.; Zhang, Q. A Two-Stage Seismic Damage Assessment Method for Small, Dense, and Imbalanced Buildings in Remote Sensing Images. *Remote Sens.* **2022**, *14*, 1012. [[CrossRef](#)]
16. Fan, X.; Scaringi, G.; Korup, O.; West, A.J.; van Westen, C.J.; Tanyas, H.; Hovius, N.; Hales, T.C.; Jibson, R.W.; Allstadt, K.; et al. Earthquake-induced chains of geologic hazards: Patterns, mechanisms, and impacts. *Rev. Geophys.* **2019**, *57*, 421–503. [[CrossRef](#)]
17. Guzzetti, F.; Mondini, A.C.; Cardinali, M.; Fiorucci, F.; Santangelo, M.; Chang, K.T. Landslide inventory maps: New tools for an old problem. *Earth-Sci. Rev.* **2012**, *112*, 42–66. [[CrossRef](#)]
18. Keefer, D.K. Investigating landslides caused by earthquakes—A historical review. *Surv. Geophys.* **2002**, *23*, 473–510. [[CrossRef](#)]
19. Van Westen, C.J.; Castellanos, E.; Kuriakose, S.L. Spatial data for landslide susceptibility, hazard, and vulnerability assessment: An overview. *Eng. Geol.* **2008**, *102*, 112–131. [[CrossRef](#)]
20. Xu, Y.R.; Allen, M.B.; Zhang, W.H.; Li, W.Q.; He, H.L. Landslide characteristics in the loess plateau, northern China. *Geomorphology* **2020**, *359*, 107150. [[CrossRef](#)]
21. Xu, Y.R.; Liu-Zeng, J.; Allen, M.B.; Zhang, W.H.; Du, P. Landslides of the 1920 Haiyuan earthquake, northern China. *Landslides* **2021**, *18*, 935–953. [[CrossRef](#)]
22. Zhang, W.H.; Xu, Y.R.; Du, P.; Li, W.Q.; Tian, Q.J.; Chen, L.Z. Interpretation of the spatial distribution characteristics of the coseismic landslides induced by the 1920 Haiyuan M 8 1/2 earthquake using remote sensing images. *Earthq. Res. China* **2020**, *34*, 523–545. [[CrossRef](#)]
23. Du, P.; Xu, Y.R.; Tian, Q.J.; Li, W.Q. Using Google Earth Images to Extract Dense Landslides Induced by Historical Earthquakes at the Southwest of Ordos, China. *Front. Earth. Sci.* **2020**, *8*, 633342. [[CrossRef](#)]
24. Du, P.; Xu, Y.R.; Tian, Q.J.; Zhang, W.H.; Liu, S. The Spatial Distribution and Attribute Parameter Statistics of Landslides Triggered by the May 12th, 2008, MW7.9 Wenchuan Earthquake. *Earthq. Res. China* **2020**, *34*, 29–49. [[CrossRef](#)]
25. Xu, Y.R.; Du, P.; Li, W.Q.; Zhang, W.H.; Tian, Q.J.; Xiong, R.W.; Wang, L. A case study on AD 1718 Tongwei M7.5 earthquake triggered landslides- Application of landslide database triggered by historical strong earthquakes on the Loess Plateau. *Chin. J. Geophys.* **2020**, *63*, 1235–1248, (In Chinese with English abstract). [[CrossRef](#)]
26. Xu, Y.R.; Liu-Zeng, J.; Allen, M.B.; Du, P.; Zhang, W.H.; Li, W.Q.; Tian, Q.J. Understanding historical earthquakes by mapping coseismic landslides in the Loess Plateau, northwest China. *Earth Surf. Process. Landf.* **2022**, 1–17. [[CrossRef](#)]
27. Lanzhou Institute of Seismology; SSB; Seismic Crew of Ningxia Hui Autonomous Region. *AD 1920 Haiyuan Great Earthquake*; Seismological Press: Beijing, China, 1980. (In Chinese)
28. Close, U.; McCormick, E. Where the mountains walked. *Natl. Geogr. Mag.* **1922**, *41*, 445–464.
29. Zhang, Z.; Wang, L. Geological Disasters in loess areas during the 1920 Haiyuan earthquake, China. *GeoJournal* **1995**, *36*, 269–274. [[CrossRef](#)]
30. Zhuang, J.Q.; Peng, J.B.; Xu, C.; Li, Z.H.; Densmore, A.; Milledge, D.; Iqbal, J.; Cui, Y.F. Distribution and characteristics of loess landslides triggered by the 1920 Haiyuan earthquake, northwest of China. *Geomorphology* **2018**, *314*, 1–12. [[CrossRef](#)]
31. Xu, C.; Tian, Y.Y.; Ma, S.Y.; Xu, X.W.; Zhou, B.G.; Wu, X.Y.; Zhuang, J.Q.; Gao, Y.X.; Wu, W.Y.; Huang, X.Q. Inventory and spatial distribution of landslides IN IX-XI high-intensity areas of 1920 Haiyuan (China) M8.5 earthquake. *J. Eng. Geol.* **2018**, *26*, 1188–1195. (In Chinese with English abstract). [[CrossRef](#)]
32. Guo, X.Y.; Fu, B.H.; Du, J.; Shi, P.L.; Li, J.X.; Li, Z.; Chen, Q.Y.; Fu, H. Monitoring and assessment for the susceptibility of landslide changes after the 2017 ms 7.0 Jiuzhaigou earthquake using the remote sensing technology. *Front. Earth Sci.* **2021**, *9*, 633117. [[CrossRef](#)]
33. Zhang, D.; Wang, G. Study of the 1920 Haiyuan earthquake-induced landslides in loess (China). *Eng. Geol.* **2007**, *94*, 76–88. [[CrossRef](#)]
34. Wang, G.H.; Zhang, D.X.; Gen, F.; Yang, J. Pore-pressure generation and fluidization in a loess landslide triggered by the 1920 Haiyuan earthquake, China: A case study. *Eng. Geol.* **2014**, *174*, 36–45. [[CrossRef](#)]
35. Pei, X.J.; Zhang, X.C.; Guo, B.; Wang, G.H.; Zhang, F.Y. Experimental case study of seismically induced loess liquefaction and landslide. *Eng. Geol.* **2017**, *223*, 23–30. [[CrossRef](#)]
36. Tapponnier, P.; Xu, Z.Q.; Roger, F.; Meyer, B.; Arnaud, N.; Wittlinger, G.; Yang, J. Oblique stepwise rise and growth of the Tibet Plateau. *Science* **2001**, *294*, 1671–1677. [[CrossRef](#)]

37. Burchfiel, B.C.; Zhang, P.Z.; Wang, Y.P.; Zhang, W.Q.; Song, F.M.; Deng, Q.D.; Molnar, P.; Royden, L. Geology of the Haiyuan fault zone, Ningxia-hui autonomous region, china, and its relation to the evolution of the northeastern margin of the Tibetan plateau. *Tectonics* **1991**, *10*, 1091–1110. [[CrossRef](#)]
38. Ren, Z.K.; Zhang, Z.Q.; Chen, T.; Yan, S.L.; Yin, J.H.; Zhang, P.Z.; Zheng, W.J.; Zhang, H.P.; Li, C.Y. Clustering of offsets on the Haiyuan fault and their relationship to paleoearthquakes. *Geol. Soc. Am. Bull.* **2015**, *128*, 3–18. [[CrossRef](#)]
39. Lanzhou Institute of Seismology; State Seismology Bureau. *Summary of Gansu Historical Earthquake Record*; Seismological Press: Beijing, China, 1989. (In Chinese)
40. Liu-Zeng, J.; Shao, Y.X.; Xie, K.J.; Yuan, D.Y.; Lei, Z.S. Variability in magnitude of paleoearthquakes revealed by trenching and historical records, along the Haiyuan Fault, China. *J. Geophys. Res.-Solid Earth* **2015**, *120*, 8304–8333. [[CrossRef](#)]
41. Han, H.; Hou, J.; Huang, M.; Li, Z.; Wang, C. Impact of soil and water conservation measures and precipitation on streamflow in the middle and lower reaches of the Hulu river basin, china. *Catena* **2020**, *195*, 104792. [[CrossRef](#)]
42. Deng, Q.D.; Zhang, P.Z.; Ran, Y.K.; Yang, X.P.; Min, W.; Chu, Q.Z. Basic characteristics of active tectonics in China. *Sci. China-Earth Sci.* **2002**, *32*, 1020–1031. (In Chinese)
43. Keefer, D.K. Statistical analysis of an earthquake-induced landslide distribution-the 1989 Loma Prieta, California event. *Eng. Geol.* **2000**, *58*, 231–249. [[CrossRef](#)]
44. Guo, X.Y.; Fu, B.H.; Du, J.; Shi, P.L.; Chen, Q.Y.; Zhang, W.Y. Applicability of Susceptibility Model for Rock and Loess Earthquake Landslides in the Eastern Tibetan Plateau. *Remote Sens.* **2021**, *13*, 2546. [[CrossRef](#)]
45. Fan, X.M.; Yunus, A.P.; Scaringi, G.; Catani, F.; Subramanian, S.S.; Xu, Q.; Huang, R.Q. Rapidly evolving controls of landslides after a strong earthquake and implications for hazard assessments. *Geophys. Res. Lett.* **2021**, *48*, e2020GL090509. [[CrossRef](#)]
46. Huang, R.Q.; Li, W.L. Research on development and distribution rules of geohazards induced by Wenchuan earthquake on 12th May 2008. *Chin. J. Rock Mech. Eng.* **2008**, *27*, 2585–2592. (In Chinese) [[CrossRef](#)]
47. Talaei, R. Landslide Susceptibility Zonation Mapping Using Logistic Regression and its Validation in Hashtchin Region, Northwest of Iran. *J. Geol. Soc. India.* **2014**, *84*, 68–86. [[CrossRef](#)]
48. Larsen, I.J.; Montgomery, D.R.; Korup, O. Landslide erosion controlled by hillslope material. *Nat. Geosci.* **2010**, *3*, 247–251. [[CrossRef](#)]
49. Wang, T.M.; Wu, J.G.; Kou, X.J.; Ge, J.P. Ecologically asynchronous agricultural practice erodes sustainability of the Loess Plateau of China. *Ecol. Appl.* **2010**, *20*, 1126–1135. [[CrossRef](#)] [[PubMed](#)]
50. Peng, J.B.; Fan, Z.J.; Wu, D.; Huang, Q.B.; Wang, Q.Y.; Zhuang, J.Q.; Che, W.Y. Landslides triggered by excavation in the loess plateau of China: A case study of Middle Pleistocene loess slopes. *J. Asian Earth Sci.* **2019**, *171*, 246–258. [[CrossRef](#)]
51. Qi, S.; Xu, Q.; Lan, H.; Zhang, B.; Liu, J. Spatial distribution analysis of landslides triggered by 2008.5.12 Wenchuan earthquake, China. *Eng. Geol.* **2010**, *116*, 95–108. [[CrossRef](#)]
52. Wang, L.M.; Wu, Z.J.; Xia, K.; Liu, K.; Wang, P.; Pu, X.W.; Li, L. Amplification of thickness and topography of loess deposit on seismic ground motion and its seismic design methods. *Soil Dyn. Earthq. Eng.* **2019**, *126*, 105090. [[CrossRef](#)]
53. Peng, J.B.; Zhuang, J.Q.; Wang, G.H.; Dai, F.C.; Zhang, F.Y.; Huang, W.L.; Xu, Q. Liquefaction of loess landslides as a consequence of irrigation. *Q. J. Eng. Geol. Hydrogeol.* **2018**, *51*, 330–337. [[CrossRef](#)]
54. Costa, J.E.; Schuster, R.L. The formation and failure of natural dams. *Geol. Soc. Am. Bull.* **1988**, *100*, 1054–1068. [[CrossRef](#)]
55. Fan, X.M.; Westen, C.J.V.; Korup, O.; Gorum, T.; Xu, Q.; Dai, F.C.; Huang, R.Q.; Wang, G.H. Transient water and sediment storage of the decaying landslide dams induced by the 2008 Wenchuan earthquake, China. *Geomorphology* **2012**, *172*, 58–68. [[CrossRef](#)]
56. Fan, X.M.; Rossiter, D.G.; Westen, C.; Xu, Q.; Gorum, T. Empirical prediction of coseismic landslide dam formation. *Earth Surf. Process. Landf.* **2014**, *39*, 1913–1926. [[CrossRef](#)]
57. Fan, X.M.; Xu, Q.; van Westen, C.J.; Huang, R.Q.; Tang, R. Characteristics and classification of landslide dams associated with the 2008 Wenchuan earthquake. *Geoenviron. Disasters* **2017**, *4*, 12. [[CrossRef](#)]
58. Guan, Y.B.; Yang, S.T.; Zhao, C.S.; Lou, H.Z.; Chen, K.; Zhang, C.B.; Wu, B.W. Monitoring long-term gully erosion and topographic thresholds in the marginal zone of the Chinese loess plateau. *Soil Tillage Res.* **2021**, *205*, 104800. [[CrossRef](#)]